



Particle-resolved hyperspectral pyrometry of metal particles

J. Hameete^{*}, M.S. Abdallah, L.C. Thijs, T.A.M. Homan, X.C. Mi, N.J. Dam, L.P.H. de Goeij

Department of Mechanical Engineering, Eindhoven University of Technology, P.O. Box 513, NL-5600 MB, Eindhoven, The Netherlands

ARTICLE INFO

Keywords:

Metal fuels
Hyperspectral pyrometry
Iron combustion
Metal dust flames
Single particle combustion

ABSTRACT

We present temperature histories of individual combusting metal particles using hyperspectral pyrometry. This method gives an increase in accuracy over traditionally used two- or three-color pyrometry, while maintaining temporal and spatial resolution. Temperatures can be determined between 1800 to > 3000 K with a precision of typically <1%. It is shown that the maximum temperature of the burning iron particles increases from 2760 K to 2840 K with an increasing mean particle size from 32 to 54 μm in air with 21 % oxygen. The relatively high temperatures and its dependence on particle size are possibly related to flow field properties of the current experimental setup. Opportunities for this method, as well as future work, are discussed.

Novelty and Significance Statement: In this article, a method to use a CCD camera and spectrograph as a hyperspectral detector, gaining a wavelength dimension while maintaining two spatial dimensions, is demonstrated and validated. This method is applied to measure the temperature of iron particles, a carbon free and circular energy carrier. This method is then used to prove that there is a particle size dependence on the maximum temperature, an open question which is often disputed in literature. This work will also add a dataset that can be used for the validation of numerical models. There are only two such datasets available for iron at this moment. Our analysis suggests that the heat release of iron is dependent on the slip velocity, possibly due to a circulating flow inside of the particle.

1. Introduction

Combustion of solid particles has been a subject of significant interest for many years, owing its importance to applications such as power generation in coal-fired power plants. Metallic particles of aluminum, boron, and magnesium have also been utilized for decades in propulsion systems for rockets and ramjets [1,2]. Lately, there has been a spike in interest with the rise of the new field of metal dust combustion, potentially replacing the need for carbon-based fuels like coal [3,4]. Iron, in particular, is a promising new fuel when it comes to energy transport and storage. The material is cheap, abundant, and it burns in air while remaining mostly in the condensed phases, making it an excellent candidate for an energy carrier that can be combusted and subsequently reduced in a cyclic manner. This metal fuel cycle can be completely carbon free if the reduction step is achieved with renewable energy [5].

To enable the wide-spread use of iron fuel, the design of new reactors is required. These reactors should have a high conversion efficiency and should be able to capture all resulting oxides for recycling. The latter means that evaporation of the iron and subsequent formation of nano-oxides should be kept to a minimum. Nano-oxides are sub-micron sized iron oxide particles that are released as a cloud when iron is combusted. The amount of iron that forms nano-oxides varies,

but can be as much as 4% [6,7]. To design these reactors, an accurate model of the combustion process of iron particles burning under various conditions (in terms of particle size, gas composition, temperature, and flow characteristics) is required. Considering the intricate interplay of numerous parameters that may influence the combustion of iron-particles, it is perhaps unwise to build an empirical database covering all of the possible conditions. Instead, a more reliable strategy would involve the development of a physics-based reaction-rate model, which holds greater promise for accurately estimating combustion characteristics such as the heat release rate (HRR). Developing such a model requires a more in-depth understanding of the fundamental mechanisms controlling the oxidation process of an iron particle at elevated temperatures. The most direct, quantitative information that can reveal the fundamental mechanism of iron combustion is the burn time and time-resolved temperature measurements obtained from single-particle combustion experiments.

The first study that attempted to experimentally study this heat release was Ning et al. In this work, burn times of single iron particles were obtained experimentally [8]. They were found to scale with oxygen concentration. In a later publication of Ning et al. the maximum temperature of particles of different sizes in different oxidation environments was determined using two-color pyrometry [9]. It was found

^{*} Corresponding author.

E-mail address: j.hameete@tue.nl (J. Hameete).

that the maximum temperature of a combusting particle is dependent on the diameter of the particle, as well as the oxygen concentration of the oxidizing gas. That work also showed that nano-oxides are formed during combustion. These nano-oxides were later found to form above temperatures of approximately 2100 K [10], and models predict that the amount of nano-oxides increases with an increase in temperature [11]. These nano-oxides were visualized in greater detail by Li et al. They found that the release of nano-oxides terminates at the peak luminosity signal, indicating that the formation of these oxides stops at the maximum temperature [12]. Ignition behavior was also studied by Li et al. Single combustion events were studied in a McKenna burner, and it was found that the particle size had a more significant effect on the combustion duration than the oxygen concentration [12]. Another study that shows time-resolved temperature measurements was recently published by Panahi et al. In their study, three-color pyrometry was used to study combustion of iron in a drop-tube furnace at different oxygen concentrations (21%, 50%, and 100%) [13].

The commonly used method to measure the temperature of solid particles is two-color pyrometry. This method was first developed for shock tube temperature measurements, but was later also used in soot temperature measurements [14,15]. Since this method is based on measuring graybody luminescence, it was adopted for the temperature measurement of burning metallic particles [9,13]. The accuracy of pyrometry measurements can be improved by increasing the number of spectral channels [16]. This improvement can be achieved by using the Bayer filter that is a part of every digital single-lens reflex (DSLR) camera [17–19]. Using multiple channels has an additional benefit of reducing the emissivity uncertainty [20]. The working principle behind dual and three-color pyrometry is briefly described as follows: Luminescence at multiple wavelengths is measured, and the luminescence intensity ratio is compared to what would be expected from a perfect blackbody to calculate the particle temperature [21].

An extension to pyrometry with multiple channels can be realized by not just taking two or three bands with distinct wavelengths into account, but an extended fraction of the electromagnetic spectrum. This method was utilized in the combustion of solid metals by Goroshin et al. [22] and more recently by Alemohammad et al. They developed a system wherein a diffraction grating was used to disperse the luminescence of burning aluminum particles. By having an imaging and a spectral channel, they were able to capture temperatures of bright, fast, sparse, and emissive particles [23].

The present work presents a technique that uses a spectrograph to create a convolution of a spectral and spatial dimension [24], using a charge-coupled device (CCD) camera as a hyperspectral detector without losing a spatial dimension. This detector employs the full 500–700 nm wavelength range to measure the time-resolved temperature of a burning iron particle as it moves through the detector field of view. This method allows for real-time, accurate temperature measurement of individual burning iron particles. The advantages of this technique over commonly used two- and three-color pyrometry techniques are the following: (1) The system is simple — any spectrograph can be used to transform a camera into a hyperspectral one that can measure a signal over a wavelength range and correlate this signal to a two-dimensional location. (2) Deviations from the graybody approximation will show up if they exist. Molecular emission can be seen as a deviation from Planck's distribution in the signal, even when it is unknown if there is molecular emission in the wavelength range of interest. In the case of iron combustion, for example, molecular emission of FeO is known to occur around 600 nm [25,26]. (3) A wavelength dimension is added without losing a spatial dimension. Most two- and three-color ratio pyrometers use photomultiplier tubes (PMTs), which enable the measurement of multiple spectral channels with multiple PMTs equipped with a filter. This type of ratio pyrometry, owing to the lack of spatial information in its measurement, poses a disadvantage when probing multiple, distinct particles. This disadvantage can be

overcome by using multiple cameras [9], but this solution increases the complexity of the experimental setup significantly.

The technique presented in this research will provide valuable insights into the combustion behavior of iron particles by introducing a new dataset. While the number of experiments on single iron particles has seen a rise in recent years, only two of the previously mentioned papers provide time-resolved temperature measurements of burning iron particles. To advance the fundamental understanding of the complex physical and chemical mechanism involved in iron particle combustion, the acquisition of more reliable temperature measurements is needed. Additionally, the development of reaction-rate models, which are essential for estimating the HRR, requires validation using multiple independently acquired experimental datasets obtained under varying conditions. The data reported in this work can serve as a resource for testing and validating these models, thus contributing to the efforts in comprehending and optimizing iron particle combustion processes.

Moreover, this study's outcomes can help address existing discrepancies in the literature, such as the different findings on the dependence of maximum temperature on particle size as reported by Ning et al. and Panahi et al. [9,13]. Additionally, the potential extension of this approach to other metallic particles opens up opportunities for further research in the field of metal dust combustion.

This paper is organized as follows: Section 2 introduces the experimental system, which is composed of an optical and a combustion system, as well as the iron particles that are used. Section 3 describes the method of temperature measurement that is used. Section 4 presents the results, which are divided into a method validation and iron particle measurements. These measurements are discussed in Section 5. Finally, Section 6 provides a conclusion.

2. Materials

2.1. Experimental setup

Fig. 1 shows a schematic of the system, which can be divided in a single particle combustion setup and an optical setup. The single particle setup consists of a burner and a dispersion system, the latter being based on the electrostatic dispersion principle that was first introduced by Shoshin & Dreizin [27]. Single particles are ejected from a central jet, which consists of a 100 μm capillary tube carrying nitrogen gas to prevent any oxidation in the jet tube, the particles are introduced to an oxidizer coflow that is electrically preheated to 1015 K, a temperature that is sufficiently high to cause the particles to auto-ignite. The velocity of the coflow is 1 m/s, while the velocity of the jet flow is 9 m/s. This velocity is chosen to prevent melting of the particle in the central jet tube, which might cause sintering of these particles to the inner walls. The amount of oxygen and the preheating temperature of the coflow can be adjusted independently. Measurements of the emission spectrum of the light emitted by the burning iron particles are performed with a spectrograph (Acton SpectraPro 300i) in combination with an intensified CCD camera (PI-MAX 4 with SB intensifier photocathode) and a Sigma 105 mm f/2.8 objective. The spectrograph has an entrance slit which, when fully open, results in a field of view at the burner of 10×45 mm. The intensified camera allows for fast, repetitive gating. In this study, a 1000 Hz repetition rate is used with an exposure time of 100 μs . Every image consists of 20 exposures, meaning that each burning particle can be captured at most 20 times in a single image. Note that we have no control over the moment when (or, for that matter, if) particles will ignite. Thus, particles may enter the field of view of the spectrograph while already burning, or leave it before burning has completed. The system also features a low power (<100 mW) 532 nm continuous wave (cw) diode laser (MGL-III-532/1), that is used for calibration of the spectral axis, as will be explained in more detail in Section 3.1. The emission by the particles in the wavelength range between 500–700 nm is captured

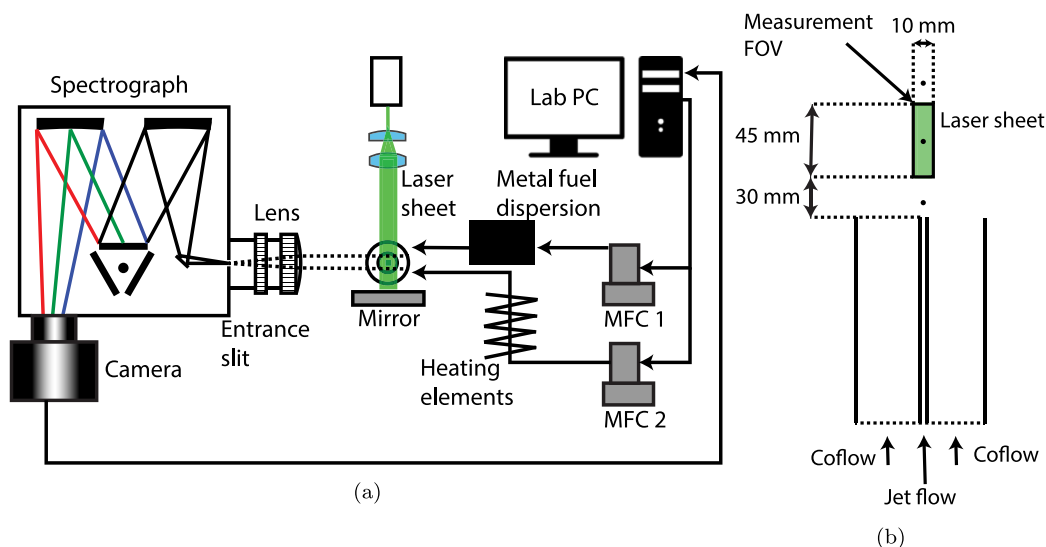


Fig. 1. (a) A schematic overview (top-view) of the experimental setup. Particles are dispersed by means of electrostatic dispersion. The feed rate depends on the current that is being fed to the dispersion system, as explained by Shoshin & Dreizin [27]. After dispersion, the particles enter a hot coflow that is electrically preheated up to 1015 K. The particles experience auto ignition and the luminescence of the particle is captured by an imaging system consisting of a spectrograph and an intensified CCD camera. (b) A side view of the camera with the measurement field-of-view (FOV). The camera detects in the range from 30 to 75 mm above the burner, but only particles that fall within the laser sheet can be used to determine the particle temperature.

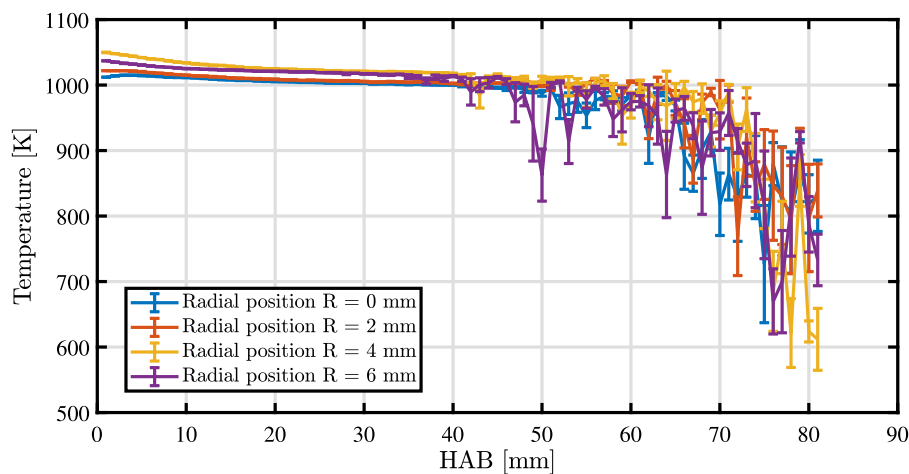


Fig. 2. Measured gas temperature profiles downstream of the burner. The gas temperature on the flow axis ($R = 0$) is almost constant up to roughly 60 mm.

with a 150 lines/mm reflection grating, resulting in a resolution of approximately 0.275 nm/pixel.

Since the flow is exposed to atmospheric conditions, the temperature of the flow in the field of view of the camera was determined. A thermocouple that scanned the flow field in the direction of the flow was used, measuring the temperature on multiple radial positions. The results of these measurements are shown in Fig. 2. It can be seen from these curves that the temperature of the flow field is uniform up to a height above the burner (HAB) of roughly 60 mm. From this point on, diffusion of heat towards the colder surrounding air decreases the mean temperature and increases the uncertainty in the surrounding temperature. The field of view of the camera ranges from HAB = 30 to 75 mm, indicating that the variation in temperature will be minimal in the first 35 mm, and a slight variation should be taken into account in the upper 10 mm.

2.2. Iron particles

The particles used in these experiments are carbonyl iron powder samples from TLS Technik which have been sieved in narrower particle size fractions than the original powder using a RETSCH AS 200

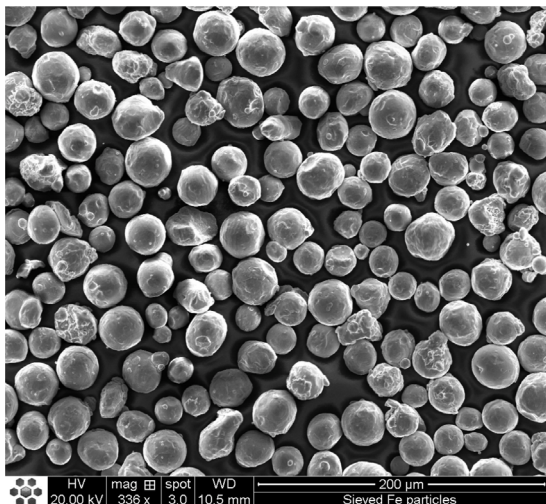
mechanical sieve. Three different sieving fractions were used in the experiments, known to be the fractions of 20–32 μm , 32–36 μm , and 45–53 μm . Particles were first studied under the electron scanning microscope (SEM). A sample of the particles in the 32–36 μm fraction is presented in Fig. 3. From the SEM image it is clear that not all particles fall in the nominal range of 32–36 μm . Multiple reasons for this discrepancy between nominal and actual sizes of sieved solid particles have been reported in Whiting et al. [28]. Thus, although sieving can be used to reduce the width of a particle size distribution, the actual distribution should be determined separately. This is especially important when comparing results of independent experiments with each other.

The particle size distribution (PSD) was measured using dynamic image analysis on a Bettersizer S3 plus. Dynamic image analysis (DIA) is a method which can measure size and provide shape information by analyzing direct images of the particles. The measured distribution of the particle diameter is presented in Fig. 4, for all three sieving fractions. This diameter is calculated based on the diameter of a sphere of equal area. All measured distributions are wider and with a larger average value than indicated by the sieving fractions. One of the reasons

Table 1

Particle size information for all three of the sieved batches.

Particle sieve range [μm]	D_{10} [μm]	D_{50} [μm]	D_{90} [μm]	D_{mean} [μm]	Circularity [-]
20–32	26.39	32.59	38.51	32.18	0.915
32–36	37.31	41.24	45.70	40.55	0.912
45–53	49.92	54.94	61.07	53.71	0.911

**Fig. 3.** SEM images of the original particles which have been sieved between 32–36 μm .

why this may occur is that sieving does not actually characterize the particles based on the diameter, but rather the minimal chord length. For convenience, particles of different size ranges will be referred to based on the nominal sieving fractions in this paper. However, Table 1 shows the particle size information of the measured batches.

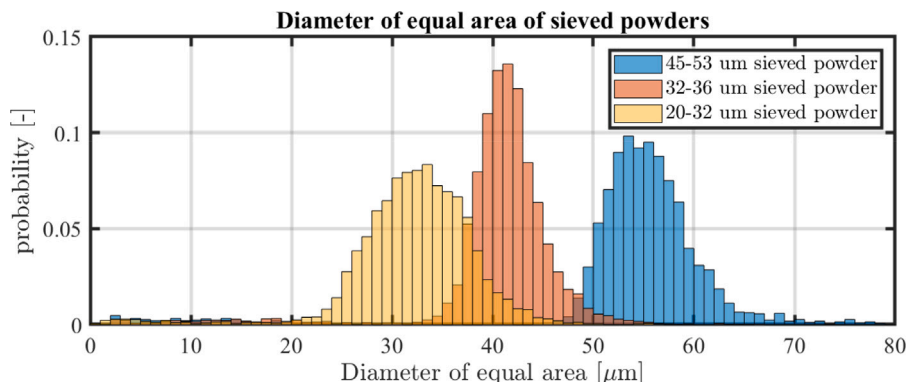
3. Temperature derivation

3.1. Signal registration

We record a continuous, 200-nm-wide stretch of the particle emission spectrum by means of an imaging spectrograph with an ICCD camera on its exit port. The camera is aligned such that pixel columns are parallel to the spectrograph entrance slit. Spectral dispersion occurs perpendicular to the entrance slit, along pixel rows. These correspond to vertical and horizontal axes, respectively, in Figs. 6(a)&(b) presented below. As discussed by Tolboom et al. each pixel row in such a device records a convolution of the spatial and spectral information present

on the entrance slit [24]. Usually, such a spectrograph is used with a narrow entrance slit, so that the spatial information is essentially a δ -function, and each pixel row records a clean spectrum. A narrow entrance slit, however, also corresponds to a narrow field of view. In our experiment, in which we aim to follow individual particles, the probability of any burning particle following a trajectory that falls within this field of view during the whole burn time is vanishingly small. In order to increase the probability of detecting full particle trajectories, we use the spectrograph with a fully open entrance slit. Since individual particles are sufficiently small to effectively represent point sources, the CCD still records a clean spectrum. However, the wavelength axis now has an offset that is unknown beforehand, because we do not know the location of the particle within the slit width. This is solved by illuminating the particles with the 532 nm diode laser. The scattered laser radiation produces a sharp peak on top of the broad gray-body spectrum, and the location of this peak fixes the wavelength axis. The laser illumination in fact solves an additional problem, viz. that of distinguishing between particles in and out of focus. The spectrograph will record any emission occurring along its line of sight. We focus the spectrograph on the burner jet axis, and are interested only in particles following the jet axis (where we know the ambient temperature, see Fig. 2). By shaping the diode laser beam into a thin light sheet, perpendicular to the line of sight of the spectrograph and comprising the burner jet axis, only particles traveling along the jet axis are illuminated and scatter 532-nm light. Other particles, when they burn, still will be recorded by the ICCD, but their spectrum will not contain a 532-nm spike. These traces are discarded.

Fig. 5 shows an example of a single particle ignition event, captured with a long exposure photograph. The lens of the spectrograph will project an in-focus particle on the entrance slit, after which its spectrum is captured during multiple exposures by the intensified CCD camera. The process of acquiring the particle temperature from an image is illustrated in Fig. 6. An example of the raw data recorded by the camera is presented in Fig. 6(a). Each horizontal band represents the spectrum of a particle at a particular HAB. The distance between subsequent horizontal bands can be used to determine the particle velocity, but that was not the purpose of the present work. At this stage, the pixel values are not yet representative of the black-body irradiance. They must first be corrected for individual pixel sensitivity variations, a so-called ‘flat field correction’. This flat field correction, in the case of a spectrograph, is different than for a bare CCD camera. The sensitivity variations are caused by a varying collection efficiency for photons

**Fig. 4.** Measured diameter of equal area for three sieve batches. The batches are labeled by their nominal size ranges, as specified by the manufacturer. The actual distributions are seen to be wider and with a larger mean diameter than the specifications.

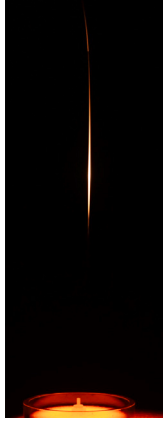


Fig. 5. A long exposure photograph of a particle moving up from the burner and experiencing auto ignition. The intensity trail is visible above the burner.

of different wavelengths of, for example, the intensifier and the lens. Therefore, the CCD needs to be calibrated using a source with a known spectrum. In this study, a tungsten lamp calibrated by the National Institute of Standards and Technology (NIST) is used. Since tungsten has a known emissivity [29], the spectrum can be calculated. Then, the measured spectrum can be compared with the theoretical spectrum to obtain an instrument function, which is a function of the wavelength. In this study, the instrument function is obtained for every pixel row to obtain a flat field correction. When this flat field correction is applied to Fig. 6(a), the resulting bands will represent a true irradiance spectrum that can be compared to a Planck distribution (Fig. 6(b)). Then, after performing the deconvolution, a Planck distribution can be fitted to the integrated signal, and the temperature of a single particle can be determined as a function of time, as is shown in Fig. 6(c).

3.2. Temperature fitting

After processing the recorded images along the procedure described above, the individual horizontal traces should be representative of the spectral intensity emitted by the burning particles. Planck's law describes the spectral distribution of electromagnetic radiation emitted by a perfect black body. Iron and iron oxide particles are assumed to be graybody emitters, with an emissivity that is lower than that of a black body ($\epsilon_{bb} = 1$), but constant over the measured wavelengths. This intensity can be described by a slightly modified version of Planck's equation:

$$I_{gb}(\lambda; T) \propto \epsilon_{gb} \frac{c_1}{\lambda^5} \frac{1}{\exp\left(\frac{c_2}{\lambda T}\right) - 1}. \quad (1)$$

In this equation, the emissivity of the gray-body emitter is denoted as ϵ_{gb} , and λ denotes the wavelength of the emitted light. The two constants c_1 and c_2 are defined as $c_1 = 2hc^2$ and $c_2 = \frac{hc}{k_B}$, where c is the speed of light, h is the Planck constant and k_B is the Boltzmann constant. Since the largest part of the emission of a graybody emitter will be far in the infrared, the entire curve cannot be recorded with the present equipment. In this work, the spectral range between $\lambda_1 = 500$ nm and $\lambda_2 = 700$ nm is recorded. Magunov, in his work, discusses the potential complication that a CCD detector is not, in fact, a power meter. A CCD detector counts photons. In many experiments this is merely a proportionality issue, but in our case the (horizontal) pixel location determines the energy of the photons they will record. Thus, the signal recorded by any pixel is not proportional to $I_{gb}(\lambda; T)$ of Eq. (1), but to $I_{gb}(\lambda; T)/(h\nu) = I_{gb}(\lambda; T) \frac{\lambda}{hc}$ [20]. This amounts to an additional wavelength dependence in the flat field correction. As shown in Appendix A, it does not really matter whether one interprets the

signal in terms of energy of photons, as long as the intensity calibration is done consistently. The validity of the graybody approximation to the combustion of iron particles is also discussed in Appendix A.

An in-house developed Matlab code was used to process the images and extract temperatures from the intensity profiles by fitting them to Eq. (1) using a non-linear least-squares approach. The only fitting parameters are the particle temperature, T and a proportionality constant, C . This proportionality constant contains the emissivity of the particle, the particle size and the collection efficiency of the detector. Since the emissivity is dependent on the temperature and the oxidation state, it cannot be determined experimentally. However, as long as the emissivity is independent on the wavelength range of interest (as detailed in Appendix A), the absolute value is irrelevant. Both of these parameters are determined with a 95% -confidence interval.

3.3. Temperature uniformity assumption

Using the method that was mentioned in the previous section, the surface temperature of a particle can be measured. The temperature uniformity can be tested with the Biot number. The Biot number indicates the uniformity of temperature in a spherical particle and is given by

$$Bi = \frac{hD_p}{6\lambda_p}, \quad (2)$$

with D_p the particle diameter, λ_p the thermal conductivity of the particle, and h the convective heat transfer coefficient, which is dependent on the Nusselt number, thermal conductivity of the gas and the diameter of the particle. Since the particle Reynolds number is smaller than 1, the Nusselt number can be assumed to be 2 [30]. In this case, the convective heat transfer coefficient can be calculated by $h = \frac{Nu \cdot \lambda}{D_p} \sim 4000$. Assuming a liquid droplet with a thermal conductivity of $38 \frac{W}{mK}$ [31], the Biot number can be assumed to be in the order of 10^{-3} . This indicates that the temperature within the particle can be considered uniform.

4. Results

In this section we first present a validation test case in which the hyperspectral pyrometer is compared to thermocouple data. Subsequently, results from single iron particle combustion are presented.

4.1. Method validation

As described in the previous section, calibration was performed using a NIST calibrated tungsten ribbon lamp. This lamp can be used as a first validation by varying the temperature of the lamp. The temperature that was used for the calibration was 2283 K. by varying the temperature of the lamp between 1804 and 2915 K, the maximum error can be obtained. An example of this is shown in Fig. 7. Here, the true temperature of the lamp is 2658 K. However, the non-least-squares fitting procedure gives a value of 2638 K, indicating that the fitted temperature is off by 20 K. An overview of these measurements is shown in Table 2.

In this table, the black-body temperature is the apparent temperature. Since tungsten is not a true black-body, the temperature needs to be corrected with the emissivity, which can be found in literature [29]. Doing so results in a true temperature, which is also reported in Table 2. The measured temperature is the temperature that was obtained with the pyrometer that is demonstrated in this work. The ΔT that is left is the difference between the true temperature and the measured temperature. The ΔT is 0 for the reference case with a true temperature of 2283 K. The ΔT is higher for high temperatures (~ 2900 K), with a maximum of 38 K. Overall, it can be seen that the error seems to increase slightly as there is a deviation from the calibrated value.

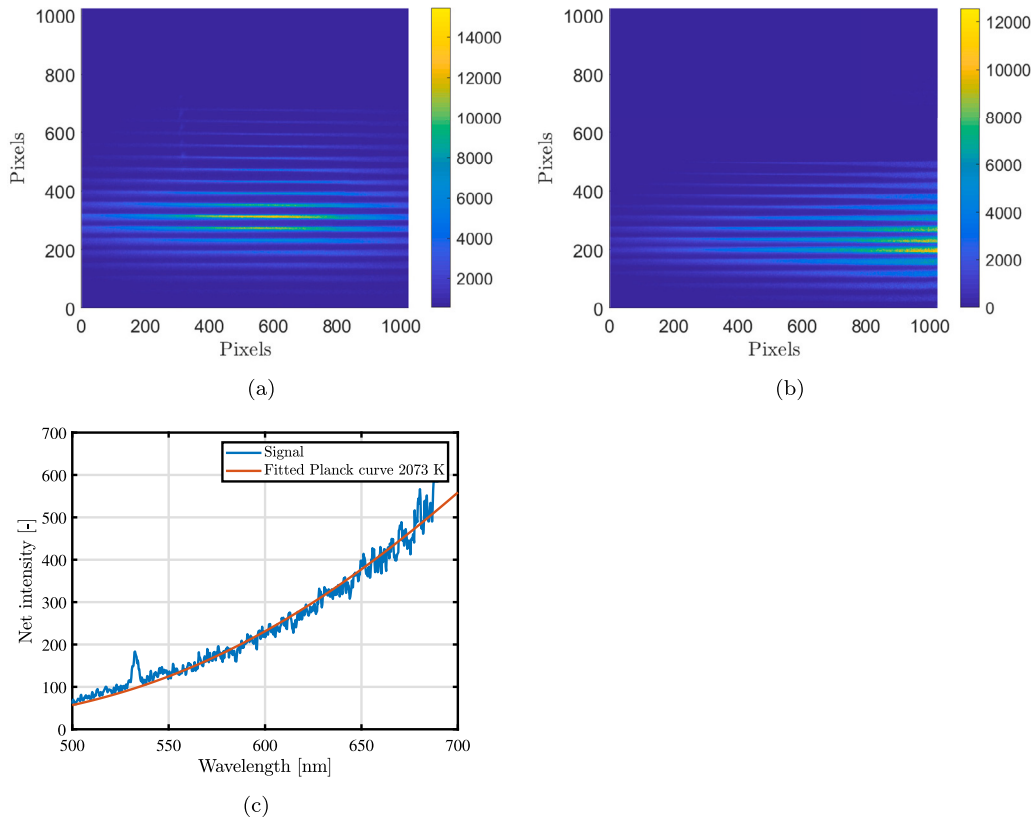


Fig. 6. The process of acquiring the temperature of a luminescent iron particle. (a) Unprocessed recording after multiple exposures. Each horizontal line corresponds to a spectrum, while the vertical direction corresponds to height above the burner. Colorbar represents pixel intensity. (b) The same data after flat-field processing, including normalization for the instrument function; the limited quantum efficiency of the available camera plays a large role here. (c) Example of a spectral intensity profile at a given HAB, integrated over the (vertical) width of the corresponding trace in (b). The temperature at each HAB can be determined from such a profile by means of non-linear least squares fitting to a Planck distribution. The peak at 532 nm is due to the green laser, as described in Section 3.1, and is masked in the fitting procedure. The good fit indicates that there is no reason to doubt the graybody assumption. (For interpretation of the references to color in this figure legend, the reader is referred to the web version of this article.)

Table 2

Validation measurements with the tungsten ribbon lamp. The black-body temperatures at different currents are measured and compared to calibration values.

Black-body temperature [K]	True temperature [K]	Measured temperature [K]	ΔT [K]
1673	1804	1797	-7
1773	1922	1914	-8
1873	2041	2037	-4
1973	2162	2162	1
2073	2283	2283	0
2173	2407	2405	-2
2273	2531	2516	-15
2373	2658	2638	-20
2473	2786	2824	38
2573	2915	2944	29

A second validation step was performed by probing a metal object with a known temperature. To this end, a K-type thermocouple with a 3-mm diameter stainless steel probe was positioned in a premixed methane-air flame. The hyperspectral pyrometer was aligned to record the emission spectrum of the thermocouple tip. The probe was allowed to reach a steady state before the measurement was performed by the thermocouple and the pyrometer. The measurement time was 20 s, by which the pyrometer could capture 100 images, while the thermocouple had captured 344 data points. These temperatures were compared, and the results can be seen in Fig. 8. Fig. 8(a) shows one of the measurements from the pyrometer. It can be seen that there is a minimal amount of noise in these measurements, and the 95% confidence interval is only 6 K. Fig. 8(b) shows the mean value and standard deviation of both measurement methods are plotted. There is

a difference of roughly 30 K between both means, which can partially be explained by the temperature gradient that will be present in the probe of the thermocouple. Since the thermocouple measures a junction within the probe, and the pyrometer only collects signal from the surface of the probe, a small deviation between the two values is expected. Overall, it can be concluded that the temperature can be determined with a high accuracy.

4.2. Single iron particle combustion measurements

Iron particle combustion measurements were performed for the three different particle size fractions in two different environments: one in atmospheric air and one in 100% oxygen. The raw single particle temperature data of the measurements of 32–36 μm particles at 21%

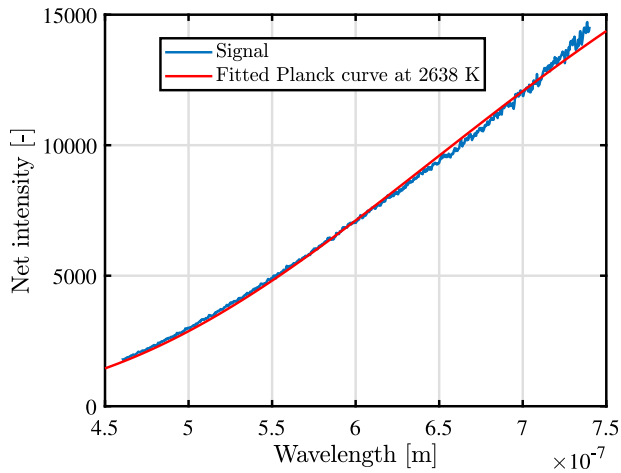
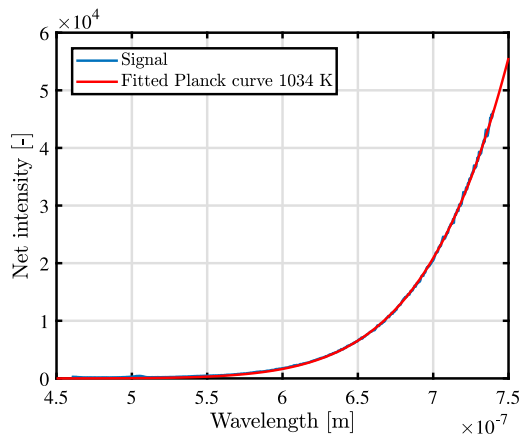


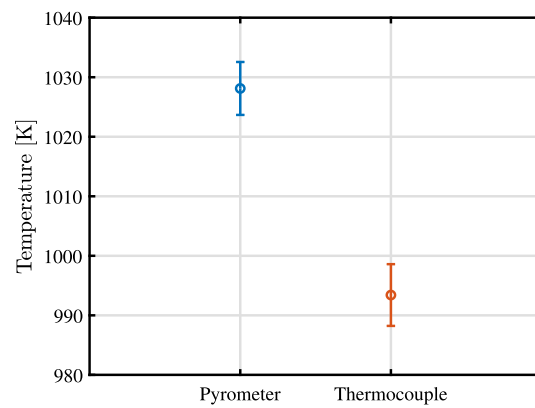
Fig. 7. Fitted Planck distribution of a tungsten ribbon lamp. The true temperature of the lamp was 2407 K, with a 95% confidence interval of 8 K.

oxygen are shown in Fig. 9. In this figure, temperature histories of 53 individual particles are plotted. Each of the lines in the plot is based on at most 20 data points; less so when particles enter or leave the field of view while already/still burning. For each curve, $t = 0$ is defined as the time where the maximum temperature was found. Data points with a coefficient of determination lower than 0.98 have been excluded from the presented data. There are multiple reasons why such points could be present, like the absence of a laser peak in the spectrum, which prevents an accurate deconvolution and will often cause an unexpected temperature jump. Most of the data points involve a temperature determined with a coefficient of determination $R^2 \geq 0.99$. Temperatures between 2000 and 3000 K are determined with 95% confidence intervals of typically ± 15 K. From Fig. 9 we infer that all particles in this batch burn with similar heating and cooling rates, reaching a maximum temperature between 2700–2900 K.

Figs. 10(a) and 10(b) show the particle temperatures of the different size ranges at atmospheric and high oxygen conditions, respectively. The solid lines represent the mean temperature of the different particle size distributions, while the gray shading represents the standard deviation (STD). Only lines where more than 20% of the maximum number of particles are still visible are shown.



(a)



(b)

Fig. 8. Comparison between thermocouple temperature measurement and the pyrometer that has been described in this work. The measurements are performed on a methane-air flame using a K-type thermocouple with a stainless steel probe. (a) A sample of the fit to the data, the 95% confidence interval of this measurement is ± 3 K. (b) the temperature difference of the thermocouple measurement and the pyrometry measurements, along with their standard deviations.

5. Discussion

5.1. Uncertainty analysis

Since there is no ground truth regarding the temperature of a burning iron particle, the current work should be carefully evaluated by the authors. Uncertainty is an important aspect in this evaluation. In this section, precision and accuracy of the results are evaluated. The precision of the measurements was already briefly discussed in Section 4.2. The mean value for R^2 is 0.9878, which corresponds with a 95% confidence interval of typically ± 15 K. This indicates a precision of typically $< 1\%$. The accuracy can be estimated using the calibration data from Table 2. As the temperature of the black-body source moves further away from the calibration temperature, the ΔT increases, up to a maximum of 38 K. This indicates that the least favorable accuracy in this calibration testing is $< 2\%$. This uncertainty reflects on the individual temperature curves as presented in Fig. 9. The standard deviation that is plotted in Figs. 10(a) and 10(b) considers the uncertainty on the temperature curve of a certain particle size range.

5.2. Absolute temperatures

Figs. 10(a) and 10(b) show that the 100% oxygen cases reach higher temperatures than the atmospheric cases. These findings are in line with the observations by Ning et al. and Panahi et al. [9,13]. Since there is more oxygen available for combustion, the oxidation occurs faster due to the increased mass transfer rate of oxygen. For the high-oxygen cases, the maximum temperature exceeds the boiling point of iron (3135K). This suggests that at least part of the iron will evaporate and burn in the gas phase. In its turn, this will increase the probability of nano-oxide formation, although the FeO shell surrounding the burning particles (FeO has a boiling point of 3400 K) will likely prevent the whole content from vaporizing. What also can be noticed from Figs. 10(a) and 10(b) is that almost no particle temperatures under ~ 1800 K have been recorded. This indicates that the recorded particles are in the liquid phase. This is most likely due to the limited detection efficiency of the system. The intensifier of the PI max camera is a Gen II SB fast gate, which is optimized for the ultraviolet, and has a maximum quantum efficiency around 280 nm which decreases gradually when it is used more towards the infrared. Since the spectral distribution of particle emission shifts to the infrared as the temperature decreases, there is a certain cut-off temperature below which particles cannot be recorded anymore. The particle temperature during cooling ($t > 0$) usually decreases below the temperature in the heating section. This

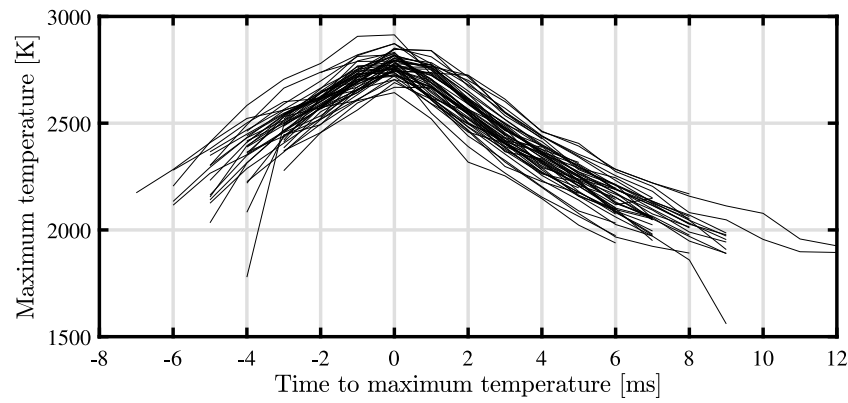


Fig. 9. Particle temperatures for the sieved batch 32 – 36 μm , combusted at 21% oxygen. Temperature was measured every ms. The individual traces are (horizontally) aligned such that $t = 0$ corresponds to them having their maximum temperature.

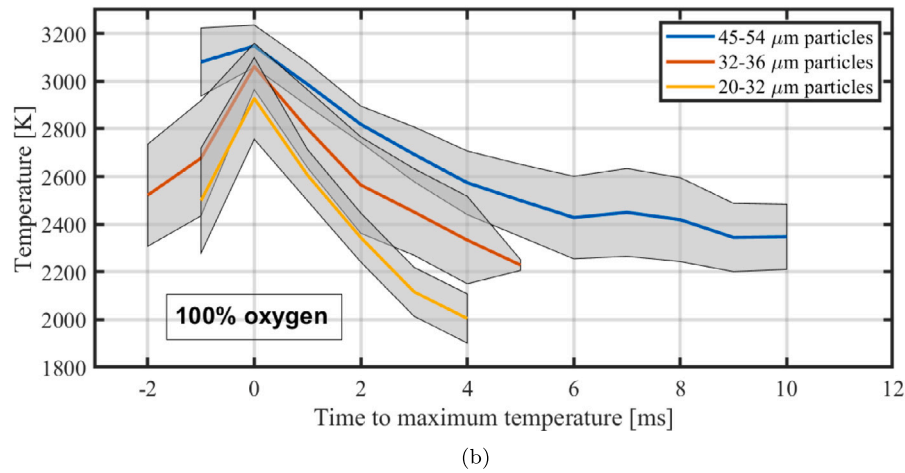
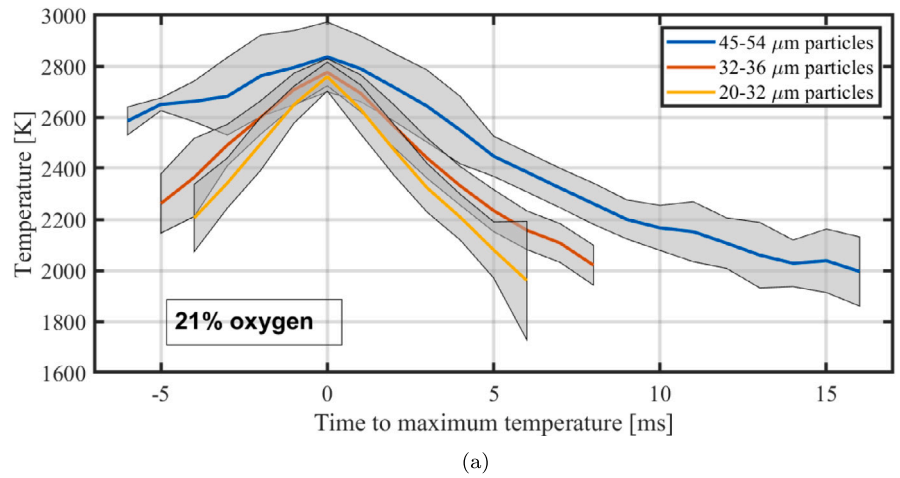


Fig. 10. Particle temperature histories for the three different size ranges. (a) Coflow of ambient air (21% O_2); (b) Coflow of 100% O_2 . Solid lines represent the mean temperature, the gray shading represents the standard deviation. $t = 0$ is defined as the time at which a particle reaches its maximum temperature.

is most likely due to ignition occurring upstream of the field of view of the camera. However, since iron oxide has an emissivity that is larger than that of iron, this could also explain that lower temperatures can be recorded after combustion.

5.3. Dependence of peak temperature on particle size

A one-way analysis of variance (ANOVA) was performed to assess the effect of particle size on the maximum temperature. The three

groups in this analysis were the three different particle sizes; the null hypothesis is that there is no effect of particle size on maximum temperature. The results from the ANOVA for the 21% oxygen case can be seen in Table 3. This table shows the sum of squares (SS), the degrees of freedom (df), the mean square (MS), the F-value (F) and the calculated P -value.

Table 3 shows a P -value of 0.0067, a value that is smaller than 0.05. This means that the alternative hypothesis, which states that there is a significant statistical difference between the three groups, can be

Table 3

ANOVA for the determination of the significance of particle size on the maximum temperature of burning iron particles in a 21% oxygen environment.

Source of variation	SS	df	MS	F	P-value
Between groups	57 847	2	28 924	5.304	0.0067
Within groups	474 404	78	5453		
Total	532 251	89			

Table 4

ANOVA for the determination of the significance of particle size on the maximum temperature of burning iron particles in a 100% oxygen environment.

Source of variation	SS	df	MS	F	P-value
Between groups	352 013	2	176 007	10.388	0.0024
Within groups	660 768	39	16 943		
Total	1 012 781	41			

accepted. This same analysis was also performed for the 100% oxygen case. This is shown in Table 4.

This table shows a P -value of 0.0024, meaning that the difference is even more significant for the 100% oxygen case. From these analyses it can be concluded that there is a significant difference in maximum temperature when the particle size is varied. From Fig. 11 it can be seen that the trend for maximum temperature is to increase with increasing particle size. This is in agreement with the findings from Ning et al. These authors argued that the increasing maximum temperature with an increasing particle size is due to less radiative heat loss for larger particles [9]. Recently, however, Thijs et al. argued that radiative heat loss actually results in the opposite trend: a decreasing maximum temperature with an increasing particle size. By examining the sensitivity of the heat release rate over the heat loss rate as a function of the particle size, written as $\frac{Q_r}{Q_l}$, the dependency of the maximum temperature on the particle size can be found. In the case of a particle burning in an external-diffusion-limited regime and considering radiative and convective heat loss, it holds $\frac{Q_r}{Q_l} \propto \frac{d_p^m}{d_m^m}$, with $m > 1$, which shows that the maximum temperature decreases as particle size increases [32]. The work of Panahi et al. does not show an increase in maximum temperature with an increasing particle size [13]. However, only two slightly different particle size fractions were studied, and the particle size distributions were not confirmed independently. It is possible that the true distributions show considerable overlap (comparable to the particles in Fig. 4), rendering any difference in T_{max} unobservable. This can also be seen in the difference in T_{max} for the smallest two particle fractions at 21% oxygen in our experiments. The difference between the mean values is only 17 Kelvin. In the next section we will discuss possible explanations for the size dependence of the maximum temperature.

5.4. Comparison to literature data

Fig. 11 summarizes the maximum temperature reached by individual particles from three different particle size distributions at the two different oxygen concentrations. Error bars represent the standard deviation of both the maximum temperature and the particle size. A comparison is made with the work by Panahi et al. who also studied the auto-ignition of single iron particles in a hot environment. The measurements from these authors were performed using a drop tube furnace heated up to a temperature of 1400 K [13], while in this work a gas temperature of 1050 K is used. The data from Panahi et al. are also included in Fig. 11. Although the experimental method of these authors is comparable to the current work in the sense that both involve a hot combustion environment, the results differ in two ways.

First, Panahi et al. did not see any significant size dependence of the maximum particle temperature. They considered two particle size fractions, one from 38–45 μm and one from 45–53 μm [13]. However,

a particle size dependency is observed in our experiments and in those of Ning et al. [9]. The statistical significance of this difference was shown in the previous section. Judging from the naming convention used by Panahi et al. for the particle size distributions, it could be that these nominally disjunct distributions are in fact showing considerable overlap.

Secondly, the peak temperatures obtained by Panahi et al. range around 2510 K [13], significantly lower than the temperatures that have been measured in the current work. However, based on the difference in gas temperatures of the two experimental set-ups, the opposite would be expected. Since the particles in the experiment of Panahi et al. burn in a hotter environment (1400 K in their work compared to 1050 K in this work) and in a closed system, it is expected that the particles will have less conductive and less radiative heat loss, resulting in a higher maximum temperature. Based on the same reasoning, it can be explained why we find higher temperatures than those reported by Ning et al. [9], since these authors performed their experiments at ambient conditions.

A possible explanation for the difference observed between the results of Panahi et al. and the results presented in this work may be found in the difference in the relative particle velocity. Panahi et al. uses a drop-tube, where the gas is stagnant, and the particles fall into the furnace injector. Therefore, there will be only a small difference between the gas and particle velocity, and the particle will quickly reach its terminal velocity (assuming Stokes drag, the response time of a 40- μm -diameter iron particle in 1000 °C air is 260 ms). This is not the case for the current setup. In this work, the velocity difference between the coflow (1 m/s) and jet flow that entrains the particles (9 m/s) is relatively large, and the particles initially experience a much larger slip velocity.

The large slip velocity could hypothetically influence the combustion of single particles in three different ways. Firstly, mass and heat transfer are enhanced with higher particle Reynolds numbers. However, due to the high gas temperature, and therefore a low gas density, the particle Reynolds number stays below one. Therefore, the impact of forced convection on the mass and heat transfer is expected to be small. Secondly, since the burning particles are molten droplets, a high slip velocity could induce a circulating flow inside the particle. This circulating flow may change the internal structure of the particle and cause more L1 (liquid iron) than L2 (liquid iron-oxide) to reach the particle surface than would be the case in low-slip conditions. This can enhance the mass accommodation of new oxygen atoms and therefore increase the maximum particle temperature [32]. Thirdly, if the particle temperature increases, part of the liquid iron is expected to evaporate and burn in the gas phase, forming a cloud of oxide nanoparticles around the burning iron particle, as discussed above. Ning et al. showed that, in a jet directing against gravity, this nano-particle cloud detaches from the particle and that the particle is lagging behind the nano-particle cloud due to the downwards settling velocity of the particle relative to the gas [10]. In the work of Panahi et al. the situation is reversed. The iron particle falls through essentially stagnant air and therefore the nano-particle cloud is lagging behind [13]. In Thijs et al. it was discussed that burning iron vapor around the particle reduces the local oxygen concentration and therefore slows down prevents the oxidation of the iron particle itself. This reduces the maximum particle temperature [11]. Since in our experiment the particles experience a significantly higher slip velocity than those in the experiments of Ning et al. and Panahi et al. it can be expected that the nano-particle cloud is more rapidly detached from our particles than from those in the other two experiments. Therefore, in our experiments the nano-particle cloud would less inhibit the diffusion of oxygen towards the micron-sized particle, which results in an increased oxidation rate and subsequently a larger maximum temperature than in the case with a smaller slip velocity. More experimental research and numerical modeling must be performed to investigate the impact of slip velocity on the combustion of single iron particles.

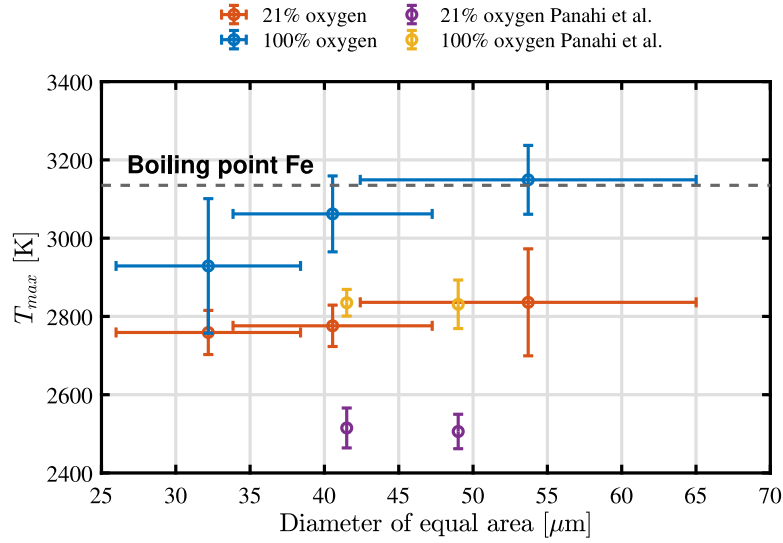


Fig. 11. Maximum particle temperatures for the three measured size fractions, temperatures for both oxygen concentrations are plotted along with error bars equal to two standard deviations on the maximum temperature and particle size. The boiling point of iron for atmospheric conditions is indicated with the black dotted line.

6. Conclusion

This work demonstrates a new method that is capable of measuring the temperature history of burning iron particles based on fitting a Planck distribution to the captured spectral luminescence distribution. The method was validated using a static thermocouple and applied to a single iron particle combustion setup. The current, non-optimized hyperspectral setup is capable of measuring temperatures between 1800 and 3200 K with a precision of ± 15 K (95% confidence interval). There is ample room for improvement. With hardware optimized for the red or near-infrared spectral range, a more intense and more informative part of the thermal emission spectrum can be captured, resulting in a still more precise temperature determination, a better time resolution, and a reduced lower temperature bound.

The system was demonstrated for three different particle size distributions, for which the temperature history was measured. We confirm the trend found by Ning et al. who showed that the maximum temperature of a particle increases with its size [9]. We tentatively attribute this size effect to the enhanced oxygen availability in situations with large slip velocities between ambient gas and iron particles. This could possibly be related to the experimental setup, as the slip velocity for this setup is much higher than that of other authors. More work is needed to investigate the impact of the ambient flow field on the maximum particle temperature.

CRediT authorship contribution statement

J. Hameete: Conceptualization, Data curation, Formal analysis, Writing – original draft. **M.S. Abdallah:** Methodology. **L.C. Thijs:** Validation, Writing – review & editing. **T.A.M. Homan:** Supervision, Writing – review & editing. **X.C. Mi:** Validation, Writing – review & editing. **N.J. Dam:** Supervision, Writing – review & editing. **L.P.H. de Goey:** Funding acquisition, Supervision, Writing – review & editing.

Declaration of competing interest

The authors declare that they have no known competing financial interests or personal relationships that could have appeared to influence the work reported in this paper.

Acknowledgments

This project has received funding from the European Research Council (ERC) under the European Union's Horizon 2020 research and innovation programme under Grant Agreement no. 884916. and Opzuid (Stimulus/European Regional Development Fund) Grant agreement No. PROJ-02594. The authors would like to express their gratitude to dr. Daoguan Ning and dr. Yuriy Shoshin for their comments and support.

Appendix A. Energy vs. photon signal derivation

Under the graybody assumption, the spectral distribution of light that is emitted by a burning metal particle is described by:

$$I_{\text{graybody}} = \epsilon \cdot \frac{c_1 \cdot \lambda^{-5}}{e^{\frac{c_2}{\lambda T}} - 1} \quad (\text{A.1})$$

Here, the signal that is captured in one pixel of the CCD detector can be treated as an energy (Eq. (A.2)) or a number of photons (Eq. (A.3)).

$$S_{\text{energy}} = A \int_t \int_{\text{pixel}} \eta_{\text{energy}}(\lambda) I_{\text{graybody}}(\lambda) d\lambda dt. \quad (\text{A.2})$$

$$S_{\text{photons}} = A \int_t \int_{\text{pixel}} \eta_{\text{photons}}(\lambda) \frac{I_{\text{graybody}}(\lambda) \lambda}{hc} d\lambda dt. \quad (\text{A.3})$$

In these equations, A is the area of a pixel and η is essentially the flat field correction. The discrepancy in these equations can be explained by the fact that a CCD sensor does not integrate incident power, but rather counts the total number of photons during the exposure time τ [20]. It is assumed that the pixels are small enough so that $\eta_{\text{energy,photons}}$ and I_{graybody} can be considered constants. Eqs. (A.2) and (A.3) can then be reduced to:

$$S_{\text{energy}} = A \eta_{\text{energy}}(\lambda) I_{\text{graybody}}(\lambda) d\lambda \tau. \quad (\text{A.4})$$

$$S_{\text{photons}} = A \eta_{\text{photons}}(\lambda) \frac{I_{\text{graybody}}(\lambda) \lambda}{hc} d\lambda \tau. \quad (\text{A.5})$$

In these equations, η_{energy} and η_{photons} are the instrument factors. Levendis et al. in their work, discussed multiple factors that may cause the recorded intensity to deviate from a Planck curve. These factors include, for example, the transmittance of the lens, and the quantum efficiency of the intensifier [16]. In the current study, the instrument function is determined by means of the spectral radiation of a NIST

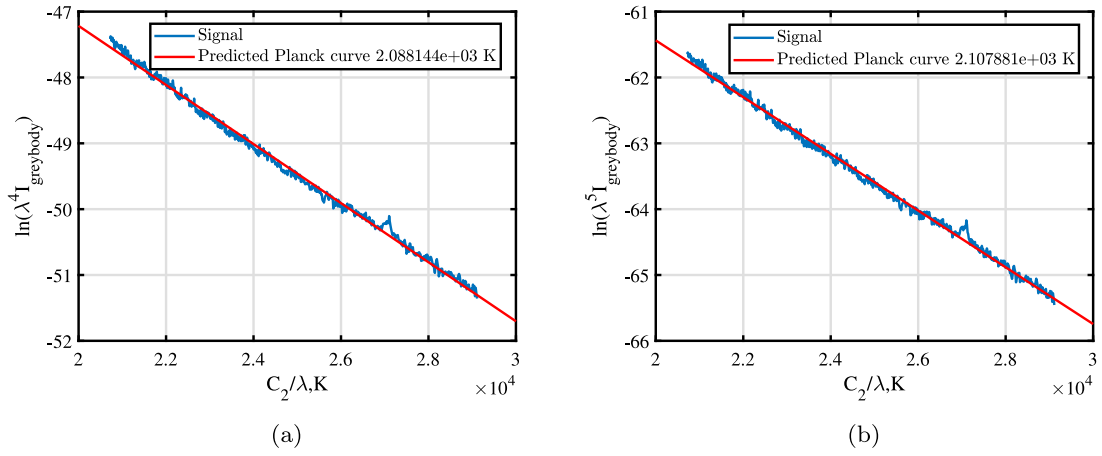


Fig. A.12. The signal of a single particle that has been processed using the two different methods. It can be seen that the resulting temperature is similar. Small deviations in the recorded temperature can be due to the noise in the signal. (a) The corrected signal that has been treated as a number of photons. (b) the corrected signal that has been treated as an energy.

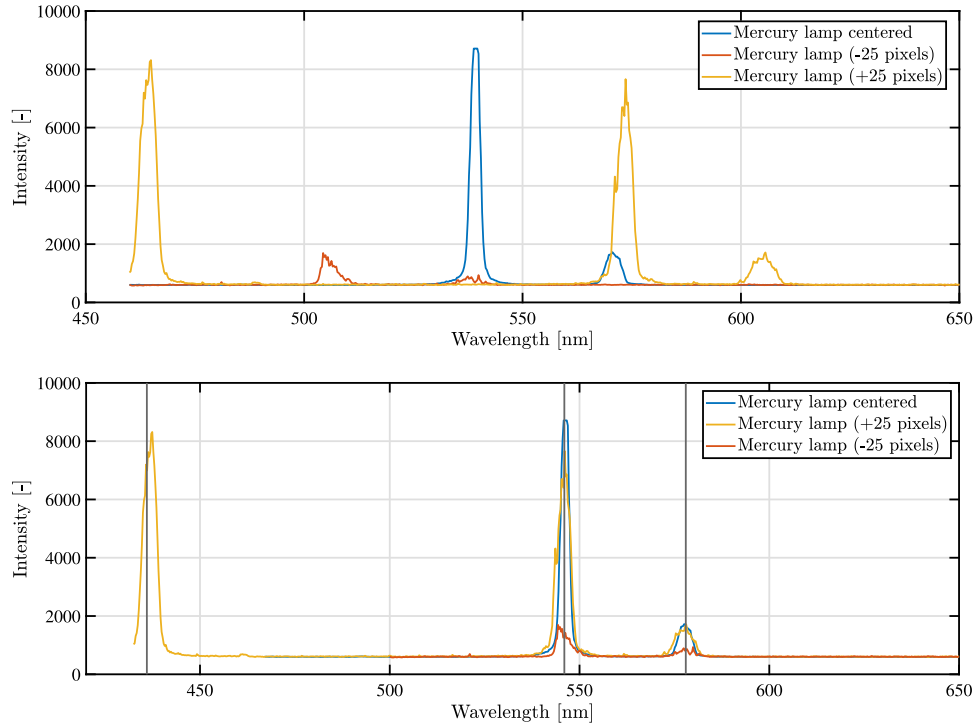


Fig. B.13. Calibration of the spectrum using a mercury lamp. The horizontal axis is calibrated for a narrow entrance slit. The three peaks that can be seen have been identified in Burns et al. [33]. When the spectra are shifted (without stretching), the peaks line up perfectly. This indicates that the spectrum does not get distorted when the particles are found off-centered on the slit.

certified tungsten strip lamp. Since the instrument function is a function of both the wavelength and the location of the image on the CCD, it is constructed by combining more than 200 images of the calibration lamp over the vertical axis of the CCD (parallel to the entrance slit). These images can then be processed to calculate an instrument function for every pixel row on the CCD. In the calibration measurements, the signal can be represented as:

$$S_{energy}^{cal} = A \eta_{energy}(\lambda) I_{Calibration}(\lambda) d\lambda \tau. \quad (A.6)$$

$$S_{photons}^{cal} = A \eta_{photons}(\lambda) \frac{I_{Calibration}(\lambda) \lambda}{hc} d\lambda \tau. \quad (A.7)$$

where the intensity $I_{Calibration}$ is known, and the instrument factors can thus be determined.

$$\eta_{energy}(\lambda) = \frac{S_{energy}^{cal}}{A I_{Calibration}(\lambda) d\lambda \tau}. \quad (A.8)$$

$$\eta_{photons}(\lambda) = \frac{S_{photons}^{cal}}{A \frac{I_{Calibration}(\lambda) \lambda}{hc} d\lambda \tau}. \quad (A.9)$$

In the current work, the signal is a photon count (S_{photon}), but it is processed as an energy (S_{energy}), so $\eta_{energy}(\lambda)$ is used as a calibration factor.

$$S \equiv S_{photons} = A \eta_{photons}(\lambda) \frac{I_{graybody}(\lambda) \lambda}{hc} d\lambda \tau. \quad (A.10)$$

$$I_{graybody}(\lambda) d\lambda = \frac{S_{photons}}{A \eta_{photons}(\lambda) \frac{\lambda}{hc} \tau}. \quad (A.11)$$

However, the signal S is treated as an S_{energy} , so the reconstruction $S \rightarrow I_{graybody}$ gives:

$$I_{graybody}^*(\lambda)d\lambda = \frac{S_{photons}}{A\eta_{energy}(\lambda)\tau} = \frac{S_{photons}}{A\eta_{photons}(\lambda)\frac{\lambda}{hc}\tau}, \quad (A.12)$$

since $\eta_{energy} = \eta_{photons}\frac{\lambda}{hc}$. So in the end; $I_{graybody}^*(\lambda)d\lambda = I_{graybody}(\lambda)d\lambda$, as long as the calibration is done consistently.

To illustrate this, a single particle at one point in time is taken as an example, and processed using both methods. Linear fitting of the corrected signal using both methods is shown in Fig. A.12 to show that there are no molecular emission lines present in the signal, and the experimental data fall on straight lines; the particle can thus be assumed to be a graybody emitter. Fig. A.12(a) shows the signal as a number of photons, while Fig. A.12(b) shows the signal as an energy. In both cases, the 95% confidence interval was less than 30 K (2075–2102K and 2095–2121K respectively).

Appendix B. Linearity correction

The linearity of the spectral shift that was explained in Section 3.1 was investigated since, in the case of non-linearities (as might be expected from a diffraction grating), the spectrum will be distorted, and may give rise to a systematic error. The validation of the linearity is done with a mercury lamp that is moved horizontally across the opening of the slit. A mercury lamp is chosen because it has well-defined spectral lines. The top of Fig. B.13 shows the spectrum of the mercury lamp at three different positions across the slit. One in the center, one shifted 25 horizontal pixels to the left, and another shifted 25 horizontal pixels to the right. Although the intensities are different, the peaks are well defined.

The bottom of Fig. B.13 shows the same lines, but shifted such that the peaks are aligned. Burns et al. describes the peaks, and finds them at the wavelengths of 492 nm, 546 nm, and 578 nm, respectively [33]. These peaks are indicated by the black lines in the figure. It is shown that when the center line (546 nm) is centered for all three spectra, the other lines are at the correct locations. This indicates that the varying location of the source (the burning particle) across the slit width does not cause any distortion of the spectrum.

References

- [1] F. Maggi, S. Dossi, C. Paravan, L.T. DeLuca, M. Liljedahl, Activated aluminum powders for space propulsion, *Powder Technol.* 270 (Part A) (2015).
- [2] E.T. Sandall, J. Kalman, J.N. Quigley, S. Munro, T.D. Hedman, A study of solid ramjet fuel containing boron–magnesium mixtures, *Propuls. Power Res.* 6 (4) (2017) 243–252.
- [3] J.M. Berghthorson, S. Goroshin, M.J. Soo, P. Julien, J. Palecka, D.L. Frost, D.J. Jarvis, Direct combustion of recyclable metal fuels for zero-carbon heat and power, *Appl. Energy* 160 (2015) 368–382.
- [4] J. Janicka, P. Debiagi, A. Scholtissek, A. Dreizler, B. Eppe, R. Pawellek, A. Maltsev, C. Hasse, The potential of retrofitting existing coal power plants: A case study for operation with green iron, *Appl. Energy* 339 (2023).
- [5] P. Julien, J.M. Berghthorson, Enabling the metal fuel economy: Green recycling of metal fuels, *Sustain. Energy Fuels* 1 (3) (2017) 615–625.
- [6] P. Tóth, Y. Ögren, A. Sepman, P. Gren, H. Wiinikka, Combustion behavior of pulverized sponge iron as a recyclable electrofuel, *Powder Technol.* 373 (2020) 210–219.
- [7] H. Wiinikka, T. Vikström, J. Wennebro, P. Toth, A. Sepman, Pulverized sponge iron, a zero-carbon and clean substitute for fossil coal in energy applications, *Energy Fuels* 32 (9) (2018) 9982–9989.
- [8] D. Ning, Y. Shoshin, J.A. van Oijen, G. Finotello, L.P.H. de Goey, Burn time and combustion regime of laser-ignited single iron particle, *Combust. Flame* 230 (2021).
- [9] D. Ning, Y. Shoshin, M. van Stiphout, J.A. van Oijen, G. Finotello, L.P.H. de Goey, Temperature and phase transitions of laser-ignited single iron particle, *Combust. Flame* 236 (2022).
- [10] D. Ning, Y. Shoshin, J.A. van Oijen, G. Finotello, L.P.H. de Goey, Critical temperature for nanoparticle cloud formation during combustion of single micron-sized iron particle, *Combust. Flame* 244 (2022).
- [11] L.C. Thijs, C.E.A.G. van Gool, W.J.S. Ramaekers, J.A. van Oijen, L.P.H. de Goey, Resolved simulations of single iron particle combustion and the release of nano-particles, *Proc. Combust. Inst.* (2022).
- [12] T. Li, F. Heck, F. Reinauer, B. Böhm, A. Dreizler, Visualizing particle melting and nanoparticle formation during single iron particle oxidation with multi-parameter optical diagnostics, *Combust. Flame* 245 (2022).
- [13] A. Panahi, D. Chang, M. Schiemann, A. Fujinawa, X.C. Mi, J.M. Berghthorson, Y.A. Levendis, Combustion behavior of single iron particles-part I: An experimental study in a drop-tube furnace under high heating rates and high temperatures, *Appl. Energy Combust. Sci.* 13 (2023).
- [14] S.B. Kormer, Optical study of the characteristics of shock-compressed condensed dielectrics, *Sov. Phys. Usp.* 11 (2) (1968) 229–254.
- [15] H. Zhao, N. Ladommatos, Optical diagnostics for soot and temperature measurement in diesel engines, *Prog. Energy Combust. Sci.* 24 (1998) 221–255.
- [16] Y.A. Levendis, K.R. Estrada, H.C. Hottel, Development of multicolor pyrometers to monitor the transient response of burning carbonaceous particles, *Rev. Sci. Instrum.* 63 (7) (1992) 3608–3622.
- [17] B.C. Connelly, S.A. Kaiser, M.D. Smooke, M.B. Long, Two-dimensional soot pyrometry with a color digital camera, in: Joint Meeting of the US Sections of the Combustion Institute. 2005, 2005.
- [18] P.B. Kuhn, B. Ma, B.C. Connelly, M.D. Smooke, M.B. Long, Soot and thin-filament pyrometry using a color digital camera, *Proc. Combust. Inst.* 33 (1) (2011) 743–750.
- [19] H. Guo, J.A. Castillo, P.B. Sunderland, Digital camera measurements of soot temperature and soot volume fraction in axisymmetric flames, *Appl. Opt.* 52 (33) (2013) 8040–8047.
- [20] A.N. Magunov, Spectral pyrometry (Review), *Instrum. Exp. Tech.* 52 (4) (2009) 451–472.
- [21] A. Araujo, Multi-spectral pyrometry - A review, 2017.
- [22] S. Goroshin, J. Mamen, A. Higgins, T. Bazyn, N. Glumac, H. Krier, Emission spectroscopy of flame fronts in aluminum suspensions, *Proc. Combust. Inst.* 31 II (2007) 2011–2019.
- [23] M. Alemohammad, E.R. Wainwright, J.R. Stroud, T.P. Weihs, M.A. Foster, Kilohertz frame rate snapshot hyperspectral imaging of metal reactive materials, *Appl. Opt.* 59 (33) (2020) 10406.
- [24] R.A.L. Tolboom, N.J. Dam, N.M. Sijtsma, J.J. Ter Meulen, Quantitative spectrally resolved imaging through a spectrograph, *Opt. Lett.* 28 (21) (2003).
- [25] P. Julien, S. Whiteley, S. Goroshin, M.J. Soo, D.L. Frost, J.M. Berghthorson, Flame structure and particle-combustion regimes in premixed methane-iron-air suspensions, *Proc. Combust. Inst.* 35 (2) (2015) 2431–2438.
- [26] Jiangqing Huang, Shen Li, David Sanned, Leilei Xu, Shijie Xu, Qian Wang, Mehdi Stiti, Yong Qian, Weiwei Cai, Edouard Berrocal, Mattias Richter, Marcus Aldén, Zhongshan Li, A detailed study on the micro-explosion of burning iron particles in hot oxidizing environments, *Combust. Flame* 238 (2022).
- [27] Y. Shoshin, E. Dreizin, Production of well-controlled laminar aerosol jets and their application for studying aerosol combustion processes, *Aerosol Sci. Technol.* 36 (9) (2002) 953–962.
- [28] J.G. Whiting, E.J. Garboczi, V.N. Tondare, J.H.J. Scott, M.A. Donmez, S.P. Moylan, A comparison of particle size distribution and morphology data acquired using lab-based and commercially available techniques: Application to stainless steel powder, *Powder Technol.* 396 (2022) 648–662.
- [29] J.C. De Vos, A new determination of the emissivity of tungsten ribbon, *Physica* 20 (7–12) (1954) 690–714.
- [30] L.C. Thijs, C.E.A.G. van Gool, W.J.S. Ramaekers, J.G.M. Kuerten, J.A. van Oijen, L.P.H. de Goey, Improvement of heat- and mass transfer modeling for single iron particles combustion using resolved simulations, *Combust. Sci. Technol.* (2022).
- [31] Marc J Assael, William A Wakeham, Arsenios Chatzimichailidis, Konstantinos D Antoniadis, Marcia L Huber, Hiroyuki Fukuyama, Reference correlations for the thermal conductivity of liquid copper, gallium, indium, iron, lead, nickel and tin **, in: High Temperatures-High Pressures, Technical report, City Publishing, 2017.
- [32] L.C. Thijs, E. Kritikos, A. Giusti, W.J.S. Ramaekers, J.A. van Oijen, L.P.H. de Goey, X.C. Mi, On the combustion of fine iron particles beyond FeO stoichiometry: Insights gained from molecular dynamics simulations, *Combust. Flame* 254 (2023).
- [33] K. Burns, K.B. Adams, J. Longwell, Interference measurements in the spectra of neon and natural mercury, *J. Opt. Soc. Am.* 40 (6) (1950).